

Numerical Simulation of a Single-tank Molten Salt Cell with Multifunctional Coupling

Ying Yang¹, Yingai Jin^{2*}, and Yanwei Sun³

^{1,2,3}National Key Laboratory of Automotive Chassis Integration and Bionics, Changchun 130022, China

^{1,2,3}College of Automotive Engineering, Jilin University, Changchun 130022, China

emails: *¹yingyang23@mails.jlu.edu.cn; *²jinya@jlu.edu.cn; and ³sunyw21@mails.jlu.edu.cn

ARTICLE INFO

Article History:

Received: 22nd June 2024

Revised: 25th September 2024

Accepted: 14th October 2024

Published: 26th December 2024

Keywords:

Single tank

Molten salt

CFD

Photovoltaic power

Heat storage

ABSTRACT

Molten salt tanks are crucial in photovoltaic power plants, serving as the core of new energy-storage systems. Although suitable for small-area domestic heating, they are complex in structure and prone to significant heat loss. To address these issues, this study proposes a novel single-tank molten salt system that combines monitoring, preheating, heat exchange, and storage functionalities. By incorporating a U-tube heat exchanger within the molten salt accumulator, the system achieves cost-effective heat storage and release. The effectiveness of the heat extraction method used with the U-tube profoundly affects the overall system performance. Through numerical simulations, this study examines the impact of different heat extraction techniques on the performance of the single-tank heat storage system, focusing on changes in the flow field within the molten salt during heat release. By modifying operational conditions, improvements in outlet temperature, heat release power, and heat utilization efficiency of the U-tube heat exchanger are demonstrated. This study explores the heat release process in a single tank of molten salt using 3D unsteady Computational Fluid Dynamics (CFD) simulations. Operation behaviour estimate results show that varied initial temperatures of the molten salt have distinct impacts on the thermal behavior of the system. Higher initial temperatures lead to a smaller temperature differential between the highest and lowest points in the tank during the same exothermic periods. And under conditions of constant inlet velocity, the exothermic power decreases as the duration of heat release increases. In scenarios with a constant inlet mass flow rate, the time required to reach the limit of exothermic power decreases as the mass flow rate increases. Throughout the exothermic process, the average heat flow density gradually declines. This decline is particularly notable in the first 10 minutes of the exothermic activity. As the process progresses, the average temperature through the heat transfer oil within the heat exchanger increases, which reduces the temperature differential between the hot and cold fluids, further decreasing the average heat flow density.

This work is licensed under a [Creative Commons Attribution-NonCommercial 4.0 International License](https://creativecommons.org/licenses/by-nc/4.0/)

1. INTRODUCTION

In recent years, China has experienced rapid growth in wind and solar power generation. However, the lagging development of the power grid has exacerbated the prominent issue of energy consumption in new energy power generation (Hou et al., 2020). Utilizing thermal storage technology to store surplus energy generated during off-peak periods or from renewable sources overnight has emerged as a viable solution for subsequent

use in daytime building heating or industrial processes (MASUZAWA, 2010). Additionally, an analysis of the shadow effect on photovoltaic arrays under varying conditions of solar radiation has been presented (Sikder et al., 2019), with results that have been experimentally verified. The successful implementation of double-tank molten-salt low-valley electric thermal storage for centralized heating serves as a model for wider adoption (Abánades et al., 2023).

In comparison to dual-tank thermal storage systems, molten salt single-tank thermal storage offers distinct advantages, including notably lower costs and suitability for heating smaller buildings during winter months. Integration of a coil heat exchanger and cylindrical partition within a single tank optimally leverages the high heat transfer coefficient of the coil and the space efficiency of the partition to effectively minimize heat storage medium mixing. This integrated approach represents an efficient method for achieving heat release from a single tank (Chen et al., 2022; Gimeno-Furio et al., 2017). The performance of the coil heat exchanger significantly influences the heat release process, prompting extensive research into coil heat exchangers within single tanks (Zhang et al., 2019).

Leo et al. (2016) modeled a two-tank molten salt thermal energy storage (TES) system under defined assumptions to describe the heat transfer between different fluids and developed a model using conservation laws. A linear quadratic control, improved by the action of observers and integrals, has been shown to be suitable for the single-tank molten-salt TES nonlinear model by simulation. The method controls the Concentrating Solar Power oil enthalpy effectively, maintaining the molten salt tank level despite variations in perturbations. Further work is to develop a model predictive control method to optimize management.

Lu et al. (2017) investigated the heat transfer process of molten salt in a cylindrical tank through simulation and experiment, obtaining data on its natural convection heat transfer. Although significant deviations occur due to its high viscosity and low thermal conductivity when using the Garon correlation, a new correlation accounting for variable physical properties was proposed, reducing the deviation to less than $\pm 20\%$. These results provide a foundation for designing a single energy storage tank. Odenthal et al. (2018) conducted a parametric study on the concept of thermocline storage of molten salts containing fillers, which achieved high implementation efficiency with minimal increases in storage volume and significant reductions in salt inventory compared to a single-tank system.

A comparative analysis by Sun et al. (2022) between two strategies in hybrid renewable energy systems outlined the best capacity determination, integrating solar PV, wind turbines, and battery storage. Compared to single-tank molten salt storage systems, thermocline packing storage exhibits only minor losses of less than 1.5%. Additionally, projections for future investment costs are very promising as it is feasible to reduce both the size of the tanks and the amount of salt used by a factor of two to three. These findings are predicated on the assumption that boundary conditions for the power block and the solar field remain constant. To refine these results further, detailed computer modeling of these components is essential. A coupled thermal performance evaluation model was proposed by Zhen et al. (2020) to evaluate heat losses and temperature distributions of the tank. The results showed that the

radiation from the air space inside the tank makes the temperature at the top of the tank equal to the temperature of the salt, so the temperature of the tank walls remains constant at different salt contents. A two-tank molten salt thermal storage system for a coal-fired cogeneration power plant was developed (Hai et al., 2020). The results demonstrate that the high and low temperatures in the two molten salt tanks have a considerable impact on the design of the components and the entropy production distribution. The temperature difference between the pinch points during the discharge duration imposes a limitation on the minimum temperature of the molten salt.

Zhang et al. (2021) presented a description of the temperature distribution in an exothermic process involving a heat storage tank with molten salt as the heat storage medium. Fluent software was employed to investigate the impact of varying heat transfer areas, structures, and layouts on temperature distribution through numerical simulation. The findings indicate that enhancing the heat exchange area can lead to enhanced temperature uniformity and heat transfer rates within the tank. Reducing the diameter of the heat exchanger tubes can mitigate the axial temperature discrepancy. When the heat exchanger is situated above the tank, it can facilitate more uniform temperature distribution and enhance heat exchange efficiency.

In the existing literature, there is a focus on comparative studies of heat storage media and configurations of single versus double tank systems, with less exploration of the different heat transfer modes in the coil heat exchanger in the molten salt tank. Leveraging commercial simulation software STAR-CCM+, this study was conducted numerical simulations to explore how different heat transfer modes within coil heat exchangers affect the heat release characteristics of molten salt in a single-tank system. The goal of this study is to provide a theoretical framework for optimizing the design of heat exchangers within single-tank systems.

2. NUMERICAL MODEL

A. Physical model

In this study, high-temperature solar salt (53% KNO_3 /40% NaNO_2 /7% NaNO_3) serves as the heat storage medium. It offers a large specific heat capacity and a wide operational temperature range, coupled with low heat storage costs. These properties enable the reduction of the storage tank's volume, thereby saving costs; the specific properties of the salt are detailed in Table 1.

THERMINOL-VP-1 is utilized as the heat extraction medium, with its physical characteristics provided in Table 2. The coil heat exchanger facilitates the direct transfer of heat from molten salt to thermal oil, which then heats cold water for building heating systems during winter via another heat exchanger. One of the focuses of this study is to investigate the heat release process as air passes through the coil heat exchanger in a single-tank molten salt configuration.

Table 1
Physical parameters of high temperature molten salt

53%KNO ₃ /40%NaNO ₂ /7%NaNO ₃	Characteristics
Melting point (°C)	142.2
Boiling (°C)	680
Maximum Allowable Membrane Temperature (°C)	620
Density (kg/m ³)	$y = -0.64T + 2209$
Dynamic viscosity (Pa·s)	$y = 6.48e-9T^4 - 1.666e-5T^3 + 0.016T^2 - 6.819T + 1092$
Thermal conductivity (W·m ⁻¹ ·K ⁻¹)	$y = 4.237e-9T^3 - 8.36e-6T^2 + 0.004906T - 0.5227$
Specific heat (J·kg ⁻¹ ·K ⁻¹)	1423.1896
Heat of melting (kJ·kg ⁻¹)	75.3453
Liquid surface tension (mN·m ⁻¹)	112
Coefficient of Expansion of Solid Salt (K ⁻¹)	0.00159
Coefficient of expansion of liquid molten salt (K ⁻¹)	0.0112
Melting point (°C)	142.2

Table 2
Physical properties of VP-1 heat transfer oil

Appearance	Clear, water-white liquid
Components	Biphenyl/biphenyl ether eutectic mixtures
Crystallization point	12°C
Moisture	300ppm
Flash point	124°C
Combustion point	127°C
Spontaneous combustion point	621°C
Specific gravity (16 °C /16 °C)	1.069
Coefficient of thermal expansion	0.000979/°C
Optimal scope of application	--
Liquid phase (chemistry)	12-400°C
Vapor phase (chemistry)	257-400°C

Figure 1 depicts the schematic diagram of the coil heat exchanger configured within a single-tank molten salt system, which integrates functions such as monitoring, preheating, heat exchange, and storage. The system features separate inlet and outlet channels for molten salt and strategically positioned thermocouples for real-time temperature monitoring. A three-stage U-tube heat exchanger is assembled internally, reducing system complexity and minimizing heat loss. At the tank's apex, a liquid level meter monitors the molten salt levels in real time. For enhanced heat exchange, a stirrer facilitates initial salt feed, and air ducts within the tank, powered by an external gas furnace-driven fan, uniformly preheat the tank, enhancing the system's efficiency and reducing investment costs.

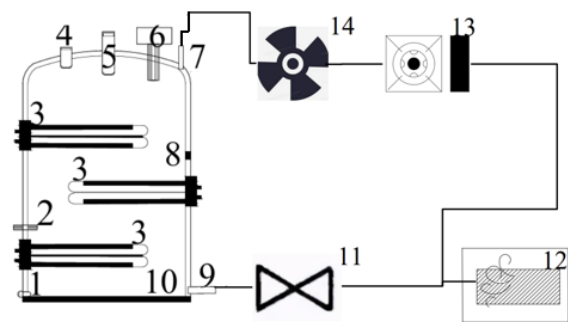


Figure 1: Molten salt storage tank integrated structure

In Figure 1, molten salt outlet; 2, thermocouple; 3, heat exchanger; 4, molten salt inlet; 5, level meter; 6, agitator;

7, circulating air inlet; 8, insulation/deflector plate; 9, circulating air outlet; 10, base plate insulation; 11, exhaust duct; 12, fresh air inlet; 13, gas furnace; 14, fan.

The coil heat exchanger is strategically placed within the bulkhead and tank wall to create a complete annular channel, adjusting the flow field distribution within the tank and improving heat release performance. This adjustment results from changes in fluid density as the molten salt cools. As air passes through the coil, it exchanges heat with the high-temperature molten salt, causing the salt in the channel to cool, increase in density, and sink. This induces a slow upward flow of warmer molten salt from the center of the tank, replenishing the annular channel (Yu et al., 2020). The natural convection process within the tank, illustrated in Figure 2, facilitates efficient heat transfer.

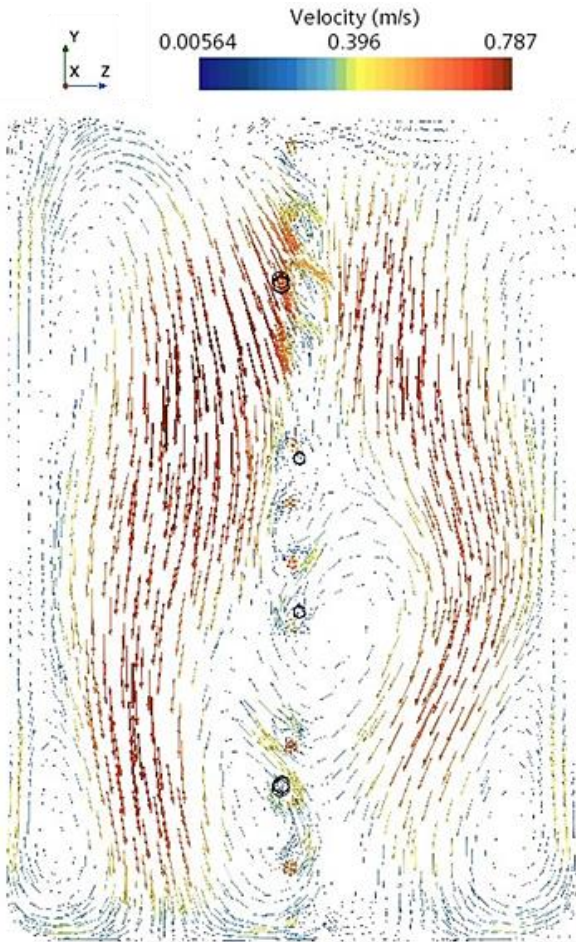


Figure 2: Vector diagram of the flow velocity of molten salt in the tank

In this study, a cylindrical tank is chosen as the physical model with a diameter of 2m and a height of 8m, excluding wall thickness considerations. The selected spiral coil heat exchanger comprises three levels, with each segment of straight pipe measuring 1.831m in length and the coil's outer diameter at 0.03m. The top, middle, and bottom heat exchanger pipes are placed at 3.708m, 2.670m, and 1.079m from the tank's bottom, respectively. The thermal insulation is 0.2m thick with a thermal conductivity of 0.0325 W/(m*K). The 3D model of the molten salt tank is depicted in Figure 3.



Figure 3: 3D model of the molten salt tank

B. Mathematical Model

The heat transfer load $Q(W)$ of the heat exchanger is calculated as:

$$Q = \frac{q_{V1}\rho_1 c_{p1}(t_{1i}-t_{0i})}{3.6} = \frac{q_{V2}\rho_2 c_{p2}(t_{1o}-t_{0o})}{3.6} \quad (1)$$

Where: c_{p1} is the specific heat capacity of the hot medium, kJ/(kg·°C); c_{p2} is the specific heat capacity of the cold medium, kJ/(kg·°C); q_{V1} is the flow rate of the hot medium, m³/h; q_{V2} is the flow rate of the cold medium, m³/h; ρ_1 is the density of the hot medium, kg/m³; ρ_2 is the density of the cold medium, kg/m³; t_{1i} is the inlet temperature of the hot medium, °C; t_{1o} is the outlet temperature of the hot medium, °C; t_{0i} is the inlet temperature of the cold medium, °C; t_{0o} is the outlet temperature of the cold medium, °C.

The enthalpy of liquid-solid film includes the latent heat of h_{fusion} :

$$h_{1s}^* = h_{1s} + (1 + Y_s^*)h_{fusion} \quad (2)$$

Where: Y is the sensible enthalpy. The relative solid-phase mass fraction is defined as the mass fraction of the liquid-solid film occupied by the solid state.

Energy conservation equations on the oil side:

$$\frac{d(c_{p_oil}m_{oil}T_{oil})}{dt} = q_{m_oil}(h_{oil_in} - h_{oil_out}) - Q_{oil} \quad (3)$$

Which:

$$h_{oil_in} = \int_{200^\circ C}^{T_{oil_in}} c_{p_oil} dT \quad (4)$$

Where: c_{p_oil} is the specific heat capacity of the heat transfer oil at the previous time step (J/(kg · K)); m_{oil} is the total mass of heat transfer oil on the tube side(kg); q_{m_oil} is the mass flow rate of heat transfer oil; h_{oil_in} is the specific enthalpy of imported heat transfer oil (J/kg) ; h_{oil_out} is the specific enthalpy of the outlet heat transfer oil (J/kg) ; Q_{oil} is the heat flow rate between the heat transfer oil and the pipe wall (W) ; T_{oil_in} is the inlet temperature of the heat transfer oil.

Energy conservation equation for the molten salt side:

$$\frac{d(c_{p_salt}m_{salt}T_{salt})}{dt} = q_{m_salt}(h_{salt_in} - h_{salt_out}) \quad (5)$$

Which:

$$h_{salt_in} = \int_{120^{\circ}C}^{T_{saltin}} c_{psalt} dT \quad (6)$$

$$h_{salt_out} = \int_{120^{\circ}C}^{T_{saltout}} c_{psalt} dT \quad (7)$$

Where: c_{p_salt} is the specific heat capacity of molten salt (J/(kg·K)); m_{salt} is the total mass of molten salt on the heat exchanger side (kg); T_{salt} is the temperature of molten salt (K); q_{m_salt} is the mass flow rate of heat transfer oil (kg/s); h_{salt_in} is the specific heat capacity of the inlet molten salt (J/kg); h_{salt_out} is the specific heat capacity of the inlet molten salt (J/kg).

3. GRID SEGMENTATION AND IRRELEVANCE VERIFICATION

A. Grid Segmentation

Based on the specified geometry and dimensions of the heat storage tank, a mathematical model is developed using meshing techniques. The 3D modeling is conducted using SolidWorks software, followed by preprocessing and meshing in the simulation software Simcenter STAR-CCM+. The mesh generator is chosen with a focus on critical aspects such as surface reconstruction, polyhedral mesh generation, automatic surface repair, generalized cylindrical mesh generation, and prismatic layer mesh generation.

During the meshing process, we configure three prismatic layers with a growth rate of 1.2 and set the thickness to 30%. Importantly, the shell component does not require observation of calculation results, thus control-face control for the prismatic layer mesh generator on the shell surface is disabled.

To enhance the fluid domain calculation results for this model, local size refinement specifically to the heat exchanger components has been applied. The optimized mesh configuration is illustrated in Figure 4, demonstrating a reasonable grid distribution and density.

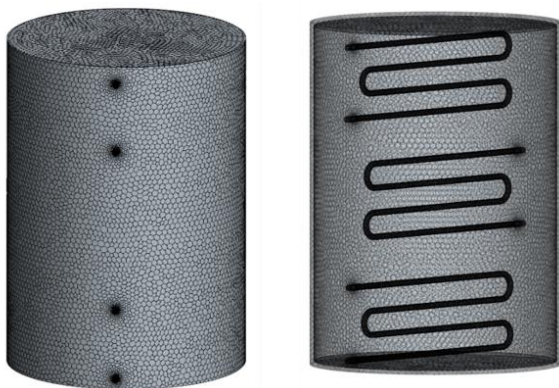


Figure 4: Molten salt tank shell and internal meshing

B. Model Validation

To validate the model's accuracy and boundary conditions, we compare simulation data with experimental results from literature. Figure 5 presents the experimental model, which

includes a single-tank heat accumulator featuring a cylindrical spacer and a coil heat exchanger. The tank is filled with molten salt and insulated with 50 mm thick aluminium magnesium silicate cotton. It measures 700mm in height (H1) and 600 mm in diameter (D1). A stainless-steel cylindrical partition with openings at both ends, measuring 300 mm in diameter (D2) and 500 mm in height (H2), is centrally positioned. The base of this partition is 90 mm from the tank's bottom (H3), creating a ring-shaped channel around it with a width of 150 mm (S). The melting solidification model used in the simulation reflects this setup to ensure comparable scaling and accurate replication of the experimental conditions. The outlet temperature variations are monitored over time and compared with experimental data to assess the model's performance.

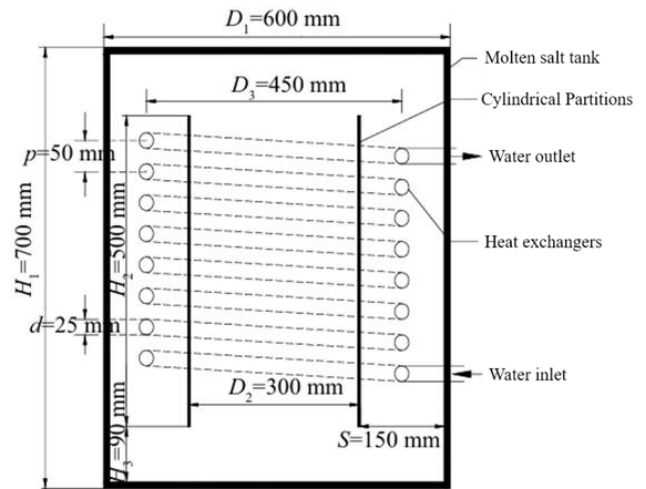


Figure 5: Single tank profile with submerged heat exchanger

As shown in Figure 6, the numerical results closely match the experimental data throughout the heat dissipation process, confirming the model's stability and reliability. Despite slight deviations in the numerical approximation of the outlet temperature—about 2.73% difference from the experimental values—these fall within the acceptable margin of error, underscoring the robustness of the simulation model used in this study.

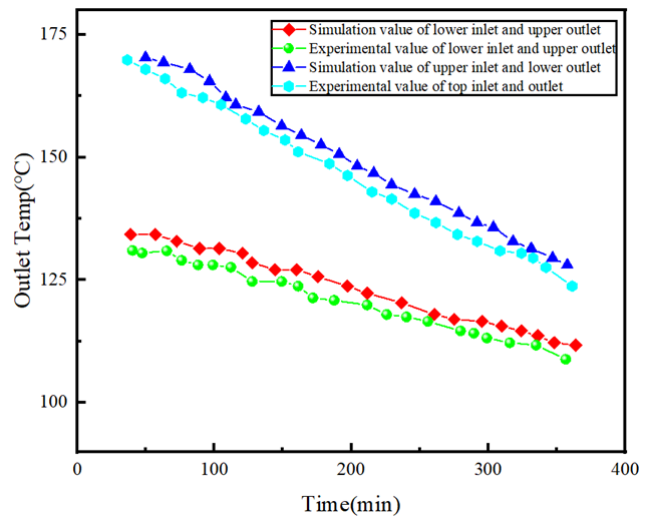


Figure 6: Comparison of simulation results with literatures' experimental results

C. Grid-independence Verification

In order to improve the accuracy of the numerical calculations, grid-independent calculations were conducted using six different grid systems. When the grid count reached 10.02×10^7 , the outlet temperature changes were minimal, indicating that this number of grids is sufficient for achieving grid-independent results. Therefore, subsequent calculations utilized a grid system containing 10.02×10^7 grids.

4. RESULTS AND DISCUSSION

A. Effect of Time on Temperature Distribution

Figure 8 illustrates the average temperature changes within the vertical cross-section of the heat storage tank's heat storage area at various stages during the heat release process. Simulations covered different moments—1 hour, 2 hours, and 3 hours—using an initial molten salt temperature of 400°C and an inlet mass flow rate of 0.2 kg/s .

During the first hour of heat release, minimal temperature dispersion is observed within the tank's molten salt, although significant temperature drops are evident near the inlet and along the pipeline during heat exchange. Despite this, the exit temperature remains high, demonstrating effective heat extraction, with temperatures ranging between 396°C and 347°C , as depicted in Figure 7(a). Extending the heat release to 2 hours, no significant vertical temperature stratification is noted. The temperatures vary from 352°C to 297°C , with notable reductions at the outlets of heat exchangers 2 and 3 due to natural convection currents within the molten salt, which drive cooler molten salt downwards (Figure 7(b)). Continuing the process for 3 hours leads to a substantial decrease in internal temperature, ranging from 327°C to 157°C , marking the completion of a comprehensive heat exchange cycle within the molten salt system (Figure 7(c)).

B. Effect of Exothermic Time on Phase Transition Situation

Furthermore, during the cooling process, molten salt undergoes a phase change into solid form once it reaches its solidification temperature. Using the relative volume fraction of solid molten salt to total molten salt (VOF model) as a reference, simulations tracked the phase transitions within the vertical cross-section of the heat storage area during the exothermic process, as shown in Figure 9.

As the duration of heat release progresses, the molten salt approaches its phase change temperature, initiating solidification within the U-tube heat exchanger and intensifying near it. At the onset of a 1-hour heat release, the temperature of the molten salt near the inlet rapidly decreases to the critical phase transition temperature of 142°C , triggering solidification. This results in the formation of a solid molten salt ring around the pipe wall, especially near the heat exchanger, as shown in Figure 8(a).

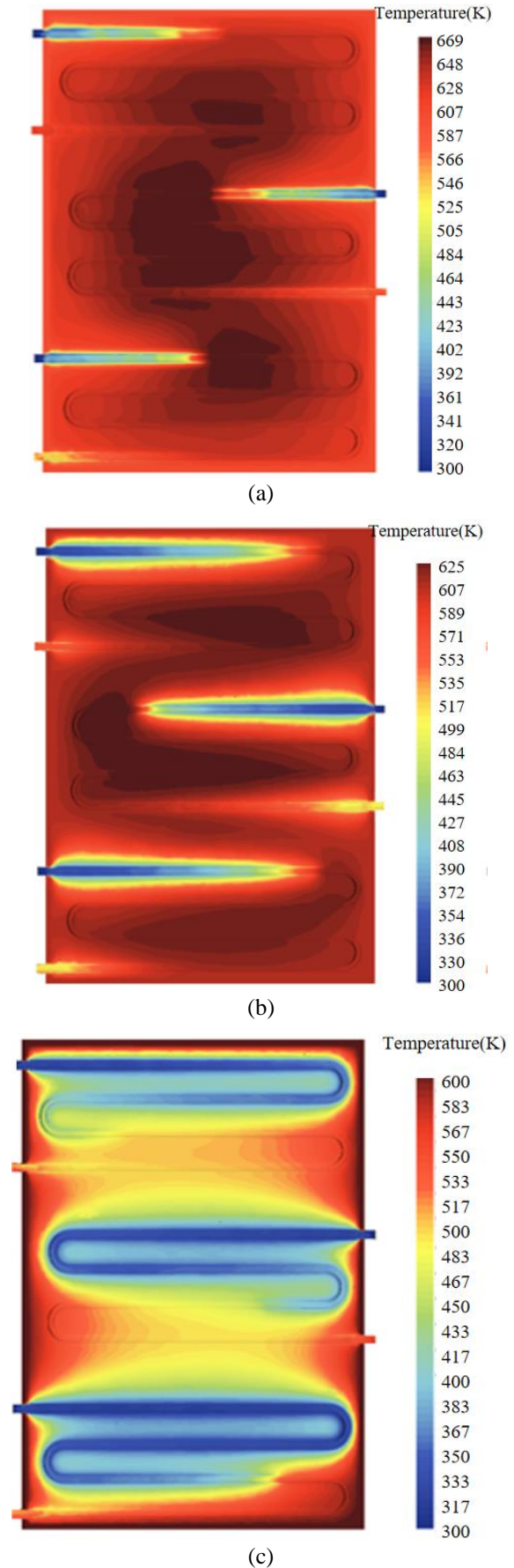


Figure 7: Temperature distribution inside the molten salt tank at different exothermic times, a) 1 hour, b) 2 hours, and c) 3 hours

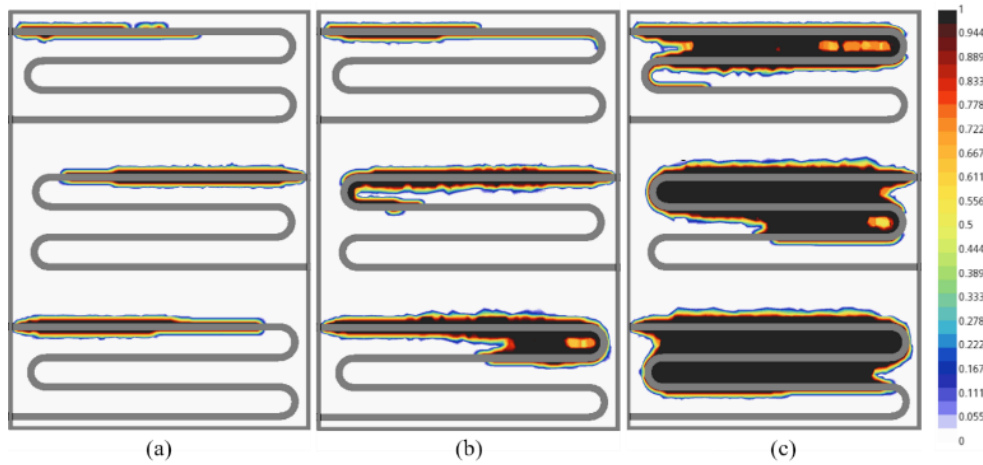


Figure 8: Phase transformation of internal molten salt under different heat transfer time conditions, a) 1 hour, b) 2 hours, and c) 3 hours

Advancing to a 2-hour heat release, the temperature near the pipe wall continues to decline rapidly due to the cooling effects of the circulating water. The denser, colder molten salt sinks toward the lower section of the tank, enhancing solidification under the heat exchanger relative to the upper sections. This creates a noticeable contrast in the visibility of phase changes between the upper and lower regions of the heat exchanger, as depicted in Figure 8(b). By the 3-hour mark, a significant portion of the molten salt near the heat exchanger has solidified. Distinct stratification between liquid and solid phases is evident, driven by natural convection and sedimentation at the base of the phase change. At this point, molten salt is

predominantly solidified, especially around the U-tube heat exchanger's exit, indicating the completion of the solidification process, as illustrated in Figure 8(c).

C. Variation of Heat Release Power at Different Inlet Mass Flow Rates

Figure 9 presents the axial average temperature distribution under different initial temperatures of molten salt. Simulations were conducted for four initial temperatures numerically 400°C, 375°C, 350°C, and 325°C that showed the average temperature distribution along the axial direction of the molten salt during the heat transfer process.

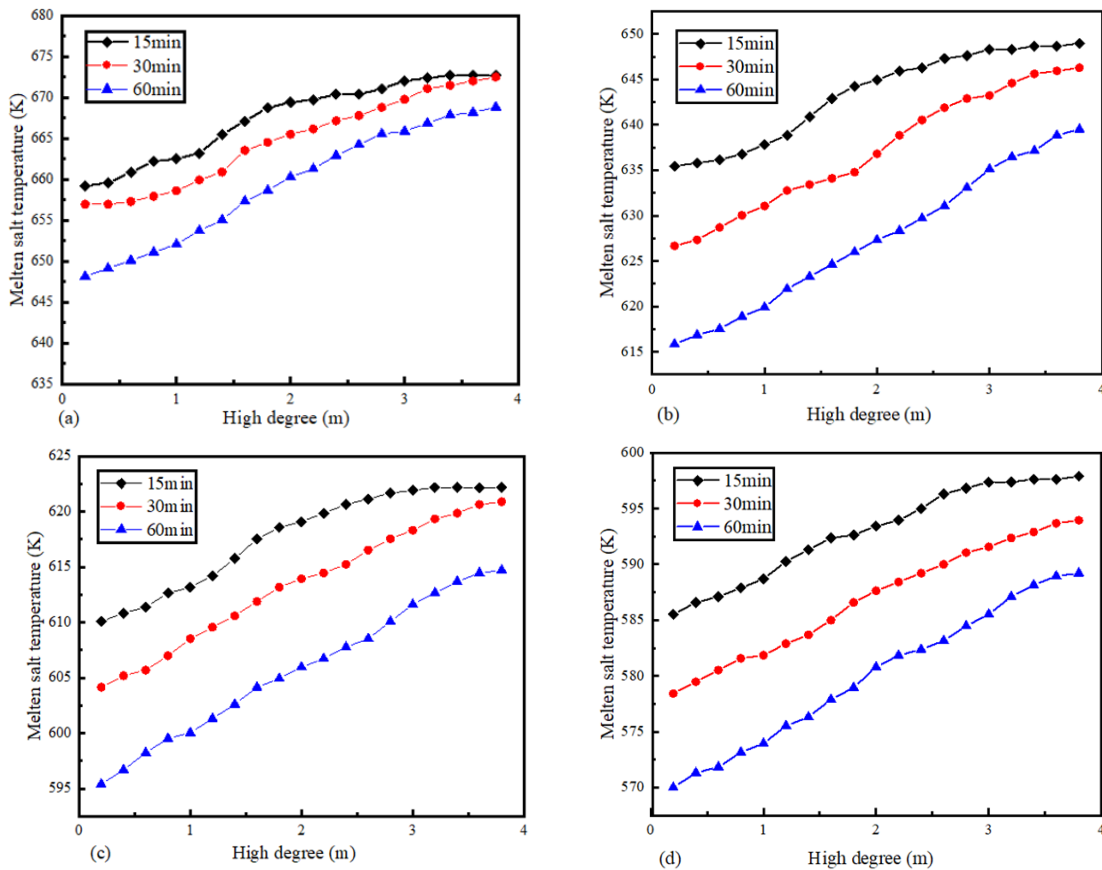


Figure 9: Axial mean temperature distribution of molten salt for heat transfer at four initial temperatures, a) 400°C, b) 375°C, c) 350°C, and d) 325°C

Figure 9 also, illustrates the impact of natural flow within the tank on the axial temperature distribution of molten salt. It is clear that the temperature of the molten salt gradually rises with height. Specifically, under 15-minute and 30-minute exothermic conditions, the temperature distribution within the tank remains relatively uniform. However, this uniformity is disrupted after a 60-minute exothermic duration, leading to noticeable temperature stratification within the tank. As the exothermic duration increases, the temperature difference between various regions within the tank progressively widens.

Further analysis shows that higher initial temperatures of molten salt result in smaller temperature differences between the highest and lowest points in the tank under the same exothermic conditions, indicating a more uniform distribution. For instance, after a 60-minute exothermic period, the temperature differences between starting temperatures of 400°C, 375°C, 350°C, and 325°C are 25.693K, 23.681K, 20.02K, and 18.877K, respectively.

Additionally, in the axial direction, the temperature change at the same position within the molten salt decreases as the initial temperature decreases under the same exothermic conditions. At a height of 1.02 m within the tank, temperature reductions after a 60-minute exothermic release are 18.947K, 15.947K, 15.877K, and 18.877K respectively, for initial temperatures of 400°C, 375°C, 350°C, and 325°C.

D. Variation of heat release power at different inlet mass flow rates

Figure 10 depicts the exothermic power under constant inlet velocity conditions. The graph clearly shows that exothermic power diminishes with increasing exothermic duration at a constant inlet velocity. Furthermore, the exothermic power peaks at a mass flow rate of $q_m=0.6\text{kg/s}$, compared to lower rates of $q_m=0.4\text{kg/s}$ and $q_m=0.2\text{kg/s}$, indicating that higher mass flow rates result in greater heat release. Using a benchmark heat release power of 335KW, the time required to reach this power varies with the mass flow rate: 2.805h for $q_m=0.6\text{kg/s}$, 3.016h for $q_m=0.4\text{kg/s}$, and 2.259h for $q_m=0.2\text{kg/s}$. Thus, a higher mass flow rate corresponds to a shorter period needed to achieve a heat release cycle and quicker attainment of the power limit.

A comparison of different mass flow rates, while keeping the inlet velocity constant, shows that the basic time required to reach the power limit of 3.066h, 3.205h, and 4.256h for $q_m=0.6\text{kg/s}$, $q_m=0.4\text{kg/s}$, and $q_m=0.2\text{kg/s}$ respectively, decreases with an increasing mass flow rate. The maximum discrepancy in heat exclusion time between the different mass flow rates is 1.19 hours.

E. Changes in Heat Flow Density During Exothermic Processes

Due to the temperature changes of molten salt in the tank, the heat flow density varies at different locations within the U-tube heat exchanger. To represent these variations, the average heat flow density across three sections of the heat exchanger is calculated, reflecting the changes in heat exchange volume throughout the exothermic process. This data is illustrated in Figure 11.

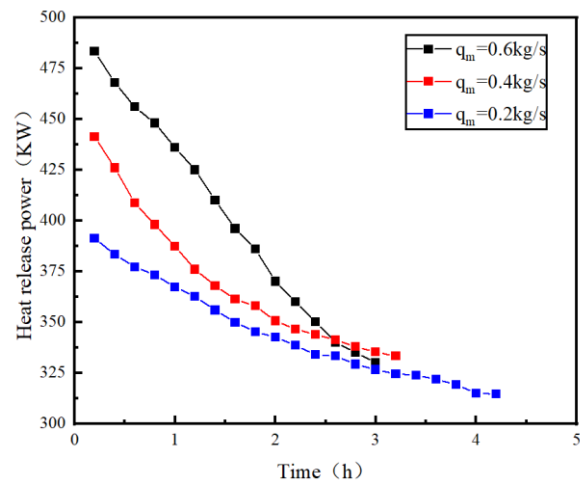


Figure 10: Heat release power at different inlet mass flow rates

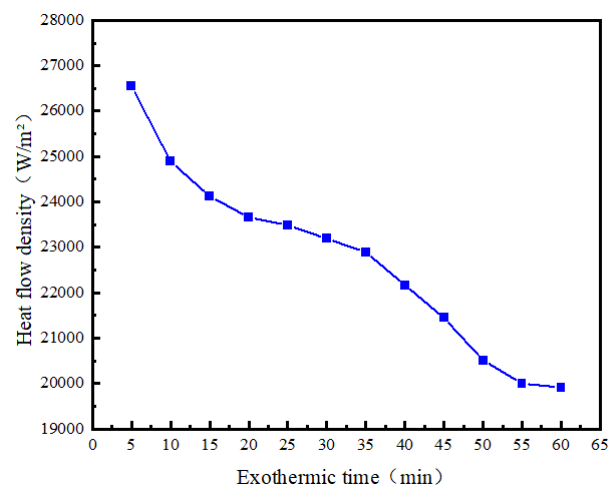


Figure 11: Variation of heat flow density of heat exchanger shell with exothermic time

From this figure, it is clear that the average heat flow density decreases over time, falling from 26552.509W/m^2 to 19914.344W/m^2 , a difference of 6638.165W/m^2 . A significant drop is noted in the first 10 minutes of the exothermic release, where the density decreases from 26552.509W/m^2 at 5 minutes to 24892.146W/m^2 at 10 minutes. This rapid decrease is likely due to the initial conditions in which the heat exchanger was charged with low-temperature thermal oil and high-temperature molten salt. The intense interaction between the cold thermal oil and the hot molten salt enhances convective heat transfer, resulting in a rapid decline in average heat flow density as the process continues. Beyond 40 minutes, the average heat flow density declines more swiftly, correlating with the cooling of molten salt in the tank. Consequently, the accumulation of cooler molten salt at the lower part of the heat exchanger speeds up the reduction in heat flow density along the tube walls.

5. CONCLUSIONS

This study explores the heat release process in a single tank of molten salt using 3D unsteady Computational Fluid Dynamics (CFD) simulations. A numerical simulation model has been developed to assess how different heat

extraction methods affect the heat release performance and the regulation of the flow field within the tank. The key findings are outlined as follows:

- Varied initial temperatures of the molten salt have distinct impacts on the thermal behavior of the system. Higher initial temperatures lead to a smaller temperature differential between the highest and lowest points in the tank during the same exothermic periods. Consequently, this results in a more uniform temperature distribution throughout the tank. Additionally, temperature differentials across different starting temperatures show a decreasing trend as the exothermic process continues.
- Under conditions of constant inlet velocity, the exothermic power decreases as the duration of heat release increases. In scenarios with a constant inlet mass flow rate, the time required to reach the limit of exothermic power decreases as the mass flow rate increases.
- Throughout the exothermic process, the average heat flow density gradually declines. This decline is particularly notable in the first 10 minutes of the exothermic activity. As the process progresses, the average temperature through the heat transfer oil within the heat exchanger increases, which reduces the temperature differential between the hot and cold fluids, further decreasing the average heat flow density.

ACKNOWLEDGEMENTS

The authors would like to express their gratitude to Changsha Automobile Innovation Research Institute Innovation Project for the financial support to conduct this work under the research on key technologies of reconfigurable photovoltaic lithium electric coupling power source for electric vehicles (CAIRIZT20220205).

REFERENCES

- Hou J. C., C. Wang C., Luo S. (2020). How to improve the competitiveness of distributed energy resources in China with blockchain technology, *Technological Forecasting and Social Change*, 151 119744.
- Masuzawa T. Energy-efficient stabilization of distributed systems with intermittent dynamics, *Kaken* (2010).
- Mostala L. M., Sikde M. S., Khan L. H., & Ridwanuzzaman K. M. (2019). Analysis of Solar Photovoltaic Array at Shadow Condition using Binary Coding method. *MIST International Journal of Science and Technology*, 2(2), 02.
- Abánades A., Rodríguez-Martín J., Roncal J. J., Caraballo A., Galindo F. (2023). Proposal of a thermocline molten salt storage tank for district heating and cooling, *Applied Thermal Engineering*, 218119309.
- Chen B. H., Shan S. Q., Liu J. Z. (2022). A novel molten salt energy storage-solar thermophotovoltaic integrated system with mid-temperature metamaterial spectrum reshaping, *Solar Energy Materials and Solar Cells*, 243.
- Gimeno-Furio A., Navarrete N., Mondragon R., Hernandez L., Martinez-Cuenca R., Cabedo L., Julia J. E. (2017). Stabilization and characterization of a nanofluid based on a eutectic mixture of diphenyl and diphenyl oxide and carbon nanoparticles under high temperature conditions, *International Journal of Heat and Mass Transfer*, 113, 908-913.
- Zhang X., Wu Y., Ma C., Meng Q., Hu X., Yang C. (2019). Experimental Study on Temperature Distribution and Heat Losses of a Molten Salt Heat Storage Tank, *Energies*, 2019.
- Leo J., Davelaar F., Besançon G., Voda A. (2016). Ieee, Modeling and control of a two-tank molten salt thermal storage for a concentrated solar plant, *European Control Conference (ECC)*, Aalborg, DENMARK, pp. 7-12.
- Wu Y. t, Li Y., Ren N., Ma C.-f. (2017). Improving the thermal properties of NaNO₃-KNO₃ for concentrating solar power by adding additives, *Solar Energy Materials and Solar Cells* 160, 263-268.
- Odenthal C., Klasing F., Bauer T. (2018). Parametric study of the thermocline filler concept based on exergy, *Journal of Energy Storage*, 17, 56-62.
- Wenyuan S., Cong T., & Yingai J. (2022). Cost and Reliability Analysis of a Hybrid Renewable Energy Systems - A Case Study on an Administration Building. *MIST International Journal of Science and Technology*, 10(3), 29-35.
- Yu Q., Lu Y. W., Zhang C. C., Wu Y. T., Sunden B. (2020). Experimental and numerical study of natural convection in bottom-heated cylindrical cavity filled with molten salt nanofluids, *Journal of Thermal Analysis and Calorimetry*, 141(3), 1207-1219.
- Zhen J. W., J J. W., Mumtaz A. (2020). Evaluation on thermal and mechanical performance of the hot tank in the two-tank molten salt heat storage system, *Applied Thermal Engineering*, 167,114775.
- Hai H. L., Shen Q., Chen Y. F. (2020). Thermodynamic Performance of Molten Salt Heat Storage System Used for Regulating Load and Supplying High Temperature Steam in Coal-Fired Cogeneration Power Plants, *E3S Web of Conferences*. 194, 1034.
- Zhang H. T., Cai L., Zhang X., Li G. H. (2021). Research on Temperature Distribution of Single Tank Using Molten Salt for Thermal Storage, *IOP Conference Series: Earth and Environmental Science*, 680, PP 012037.